lubricants

MDPI

Article

The Influence of Friction Parameters and Material Type on Results in the Block-on-Ring Friction System

Marcin Madej [1,*] and Beata Leszczyńska-Madej [2,*]

[1] Faculty of Metals Engineering and Industrial Computer Science, AGH University of Krakow, 30 Mickiewicza Ave, 30-059 Krakow, Poland
[2] Faculty of Non-Ferrous Metals, AGH University of Krakow, 30 Mickiewicza Ave, 30-059 Krakow, Poland
* Correspondence: mmadej@agh.edu.pl (M.M.); bleszcz@agh.edu.pl (B.L.-M.)

Abstract: The block-on-ring friction system is one of the more universal methods of measuring the tribological properties of materials, where we are able to compare the properties of different materials using a prescribed counter sample. When preparing for a test, we usually determine the parameters that appear to be optimal for testing a given material for its applications. The question remains whether and how such a choice affects the results obtained. In this paper, tests have been carried out on two commonly used plain bearing alloys, B83 and B89. The T-05 tester used for the tests allows the rotation of the counter sample to be adjusted, and, in this study, this was varied in the range of 50, 100, 150, 200 and 250 rpm. Another parameter variable in the tests was the friction distance, and two distances of 100 and 250 m were used. As the tests were carried out under technically dry friction conditions, it was possible to capture both the effect of the running-in period and the stable friction path. The tests showed that the alloys tested over the longer friction distance of 250 m responded differently to a change in parameters, with alloy B83 showing a sinusoidal variation in wear resistance with a maximum at medium speed, whereas alloy B89 is characterized by a continuous increase in wear with increasing speed. The coefficient of friction is more dependent on speed, and the basic conclusion can be drawn that increasing speed results in a lower coefficient of friction. This research has confirmed the need for the careful selection of test parameters and the difficulty of comparing results when there is even a slight difference in the test parameters used at different test centers.

Keywords: tribology; block-on-ring test; test parameters; bearing alloys

Received: 4 February 2025
Revised: 12 February 2025
Accepted: 18 February 2025
Published: 19 February 2025

Citation: Madej, M.; Leszczyńska-Madej, B. The Influence of Friction Parameters and Material Type on Results in the Block-on-Ring Friction System. *Lubricants* **2025**, *13*, 94. https://doi.org/10.3390/lubricants13020094

1. Introduction

The block-on-ring tribotester is used to assess the wear resistance of metals and plastics during friction. It can also be used to study the lubricating properties of greases, oils, and solid lubricants, as well as to examine the scuffing resistance of coatings. The test assembly consists of a stationary sample (block) made of the material under investigation, pressed with a predetermined force P against a counter sample, which is a rotating roller moving at a set speed in one direction. Selected tester models additionally perform an oscillatory (reversing) motion with an appropriate frequency and amplitude. The tested contact can be concentrated (linear) or distributed.

Due to its structural solutions and equipment, the device allows tests to be conducted under both technically dry and lubricated sliding conditions, with a wide range of sliding speed adjustments. The friction pair can also be placed inside a tank equipped with a heating element, enabling the test oil to be preheated to a set temperature before sliding

contact. Because the contact can be concentrated or distributed, the tribological contact area changes as wear progresses, which affects the obtained results. The operation of the tester has been described, for example, in the publication by Li and Leroux for Nanovea [1].

The literature contains publications in which authors attempt to establish correlations between various parameters related to tribological tests and the obtained results. Fehim [2] reviewed the typical wear behaviors of representative metallic alloys, ceramics, polymeric materials, and composites concerning their wear performance over time. Additionally, a predictive wear modeling approach was presented, demonstrating the influence of different friction pairs on the obtained properties. A different approach was presented by Abhishek [3], who indicated that, in metal-composite materials reinforced with non-oxide particles, oxidative wear plays a major role in the overall material degradation and removal process. The study emphasized that designing new materials with increased resistance to oxidative wear requires understanding the impact of operating parameters on wear resistance. For this reason, an analytical model was proposed to predict the relationship between oxidative wear volume, load, and sliding speed.

Chavhan and Wankhade demonstrated that parameters based on process conditions and material composition, such as steel volume %, sliding distance, and applied load, were identified as factors influencing the wear of composite samples [4]. To assess the influence of these parameters, Taguchi and ANOVA techniques were employed. The analysis of experimental data revealed that SWR and the average CoF increased with rising sliding distance and load, whereas they decreased with an increase in steel volume %. Research has also been conducted on the tribological behavior of carbon fiber-reinforced polymer composites under boundary lubrication [5]. Experiments were carried out in two directions: one with varying normal loads from 6 to 16 N and another at a low sliding speed of 110 mm/min under boundary lubrication conditions. The obtained results indicate that, within the observed range, the influence of normal load and sliding velocity resulted in relatively low friction coefficients and shallow wear depths. Muratov et al. investigated the effects of friction, temperature, and sliding velocity on the tribochemistry of silicon nitride [6]. The temperature dependence of the wear rate of silicon nitride was studied in different solutions. As the temperature increased, the material removal rate decreased, and these changes were accompanied by corresponding variations in the coefficient of friction. Another perspective on the impact of parameters on test results is provided by authors of publications [7,8], who demonstrated that friction parameter values obtained from devices where the contact area is a few square millimeters cannot be applied to cases where the real contact area is only a few micro- or nanometers squared.

Cemented carbide cutting tools are still widely used in machining processes due to their wear resistance. The objective of the authors in publication [9] was to study the wear mechanisms of WC-Co cutting tools under varying tribological conditions. Dry friction experiments were conducted using a high-speed pin-on-disk tribometer over a wide sliding speed range (60–600 m/min). The results showed the wear rate under different tribological conditions, the evolution of the coefficient of friction and temperature as a function of sliding speed, and the development of wear mechanisms. Significant differences in wear mechanisms were observed depending on test speed and the circulation of contaminants in the friction contact zone.

Zhen et al. [10] investigated the tribological behavior of a nickel-alloy-based self-lubricating composite (82.5% Ni-alloy–12.5% Ag–5% BaF_2/CaF_2) against a Si_3N_4 ball under various temperatures and sliding speeds. Results showed that the coefficient of friction and the wear rate of the composite were significantly dependent on testing temperature and sliding speed. Jansons et al. presented the correlation between tribological and mechanical properties of NSC, as well as its surface texture, to determine the extent to which

surface texture influences the tribological performance of coated workpieces. Additionally, the measuring and evaluation procedure of nano-coatings was analyzed [11]. A strong correlation was observed between steady-state dry sliding friction, CoF, and the amplitude and functional surface texture parameters of the tribo-track. The authors of publication [12] examined the coefficient of friction of anodic oxide layers formed on Al5754 under varying normal loads, sliding speeds, and oxide thicknesses using a pin-on-disk tribometer. The results indicated that both the load and sliding speed had an increasing effect on the coefficient of friction.

Bearing alloys remain an attractive research material, and comparisons of the properties of different alloys are frequently found in the literature [13–16]. There are also studies on the effects of lead additions on the properties of babbitts [17] and even the application of babbitts as composite materials [18–21]. For bearing alloys, researchers have examined the possibility of improving the wear resistance of bare babbitt modified with CuLa and evaluating the effects of different sliding modes on its tribological properties [22]. The tribological properties of unmodified and modified babbitt were assessed under both reciprocating and unidirectional sliding conditions in a lubricated environment. The study demonstrated that anti-friction properties and wear resistance under reciprocating mode were superior to those under unidirectional mode. Branagan [23] compiled efforts to understand the sources and consequences of damage in industrial babbitted bearings, which operate under hydrodynamic or hydrostatic film lubrication. The study discusses major types of damage within broader damage categories.

Despite numerous studies analyzing the tribological properties of bearing alloys, there remains a significant gap in understanding how variations in friction parameters in-fluence the comparability of test results in block-on-ring systems. Previous research has extensively focused on material compositions, lubrication conditions, and specific wear mechanisms, yet the impact of rotational speed and sliding distance variations on the wear behavior of different bearing alloys under dry friction remains underexplored.

The current study addresses this gap by systematically investigating two commonly used bearing alloys, B83 and B89, under controlled variations in rotational speed and friction distance. By analyzing the tribological responses over short and extended friction paths, we reveal how different materials react to changes in test parameters and how these variations influence wear resistance and coefficients of friction. This approach enables a deeper understanding of the testing methodology's limitations and provides a framework for improving result comparability across different testing centers.

2. Materials and Methods

Two types of commercially available tin-based bearing alloys, SnSb11Cu6 (B83) and SnSb8Cu4 (B89), were used as the material for this study. These alloys are commonly employed in the casting of plain bearing shells. The casting process involved pouring the alloys into cast-iron molds, followed by air cooling. The chemical composition of the tested alloys is presented in Table 1.

Table 1. Chemical composition of the investigated alloys, wt%.

Name of Alloy		Chemical Composition			
Grade Mark	**Designation**	**Sn**	**Pb**	**Sb**	**Cu**
SnSb11Cu6	B83	Rest	-	10.76	4.96
SnSb9Cu4	B89	Rest	0.21	7.62	3.91

The loss of mass during the test related to the test parameters with special emphasis on the rotation speed of the counter sample was presented as the wear rate and determined according to Equation (1):

$$w_r = \frac{\Delta m}{L \cdot t} \quad (1)$$

where

Δm—Loss of mass [g];

L—Load [N];

t—Test time [s].

A constant load of 50N was used for the tests. The load applied is similar to that encountered in industrial conditions when the alloys tested are used in bearings.

Tin-based bearing alloys exhibit excellent lubricity, ductility, and corrosion resistance. They are distinguished by their high fatigue strength and abrasion resistance, making them suitable for applications involving high linear speeds and heavy loads. The tribological properties were evaluated using a T-05 block-on-ring tribotester (Łukasiewicz—ITeE, Radom, Poland) (Figure 1) at an ambient temperature of 21 °C under technically dry friction conditions. During the test, in order to ensure proper contact between the specimen and the steel ring (heat-treated steel 100Cr6, 55 HRC, Ø49.5 × 8 mm) rotating at a constant speed, a rectangular tribological sample (4 × 4 × 20 mm) was fixed in a holder containing a hemispherical insert. The surface of the specimen in contact with the friction was oriented perpendicular to the direction of the load (L). A double lever system was employed to apply the load in the direction of the ring, with a load accuracy of ±1.5%.

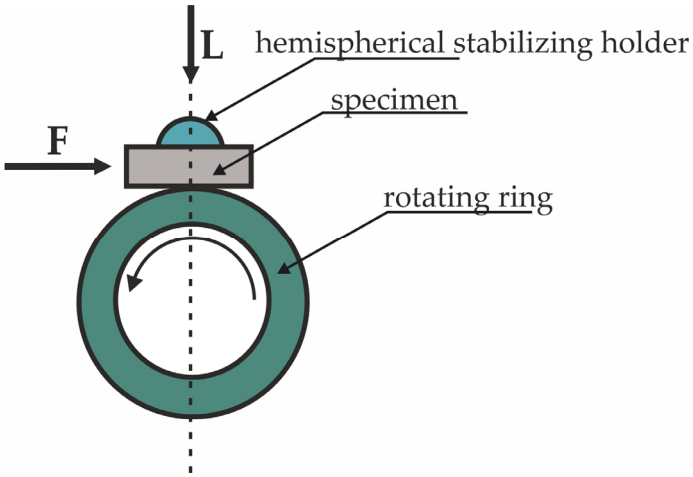

Figure 1. Schematical diagram of the T-05 block-on-ring tribotester; F—friction force measurement; and L—load perpendicular to the friction surface [24].

Table 2 presents the friction process parameters used in this study. A minimum of three tribological tests were conducted for each of the materials examined.

Table 2. The wear test parameters.

Sliding Contact	Counter Sample	Rotational Speed	Load	Sliding Distance
Technical dry	steel 100Cr6, heat-treated, with hardness 55 HRC	50 rpm 100 rpm 150 rpm 200 rpm 250 rpm	50N	100 m 250 m

The microstructure of the specimens analyzed in this study was examined using an OLYMPUS GX51 light microscope (Olympus, Tokyo, Japan) and a Hitachi SU 70 scanning electron microscope equipped with a Schottky-type thermal field emission electron gun (FESEM) (Hitachi, Tokyo, Japan). Hardness testing was performed using a Brinell hardness tester with a force of 31.25 kg and a 2.5 mm carbide ball, in accordance with the ASTM E10-18 standard [25]. The hardness values measured were 24 ± 1.1 HB for alloy B83 and 20 ± 0.6 HB for alloy B89.

Figures 2 and 3 present representative results from the microstructure analysis. The microstructure of the B83 alloy displays a substantial quantity of large rhomboidal and cubic SnSb phase precipitates, along with numerous needle-like and almost globular Cu_6Sn_5 phase precipitates. The matrix consists of a solution of antimony and copper within tin (Figure 2). In comparison, the microstructure of the B89 alloy shows fewer rhomboidal SnSb phase precipitates, while, like the B83 alloy, it also contains needle-like and nearly globular Cu_6Sn_5 phase precipitates (Figure 3). Comprehensive results regarding the microstructure of the analyzed alloys were discussed in the authors' previous publications as well as in those of other researchers [26–31].

(**a**) (**b**)

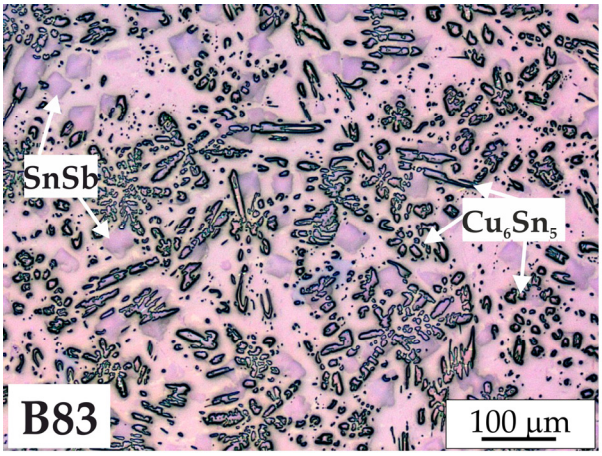

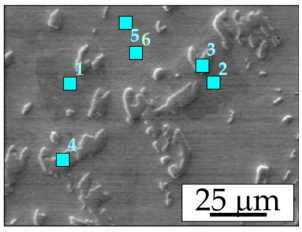

wt. %	Cu	Sn	Sb
1		57.24	42.76
2		57.69	42.31
3	42.18	57.82	
4	42.70	57.30	
5	0.09	96.23	3.68
6		96.09	3.91

Figure 2. Microstructure of the B83 bearing alloy: (**a**) light microscope photograph, (**b**) microstructure and results of point chemical composition analysis, and photograph made using a scanning electron microscope.

(**a**) (**b**)

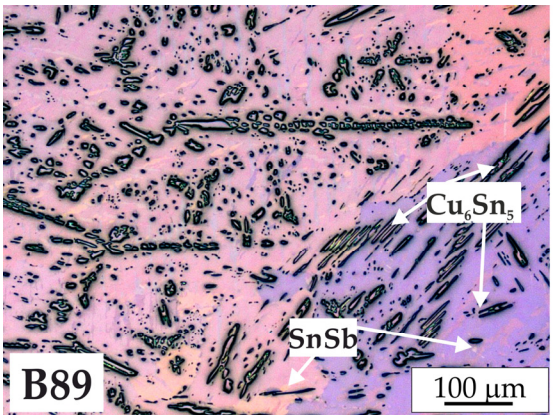

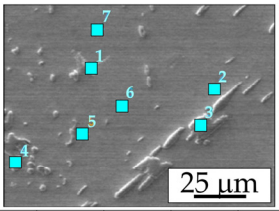

wt. %	Cu	Sn	Sb	Pb
1		11.91		86.09
2		68.02	31.98	
3	41.99	58.01		
4	41.04	58.98		
5		97.11	2.89	
6		86.70	13.30	
7		97.84	2.16	

Figure 3. Microstructure of the B89 bearing alloy: (**a**) light microscope photograph, (**b**) microstructure and results of point chemical composition analysis, and photograph made using a scanning electron microscope.

3. Results

This study was conducted to examine the impact of the T-05 friction process parameters on the wear resistance and friction behavior of the bearing alloys (B83 and B89) against a steel 100 Cr6 friction counter sample.

The rotational speed was variable, firstly, to show its influence on the wear resistance of the alloys tested, and, secondly, to check whether changing the rotational speed of the test specimen affected the results obtained, as it is extremely rare that we are able to match the rotational speed to the real working conditions. The friction distance was also a variable factor; two friction distances were used: 100 and 250 m. The longer distance helped to highlight the influence of the steady state period on the results obtained at the expense of the linear part of the friction.

Figures 4 and 5 show the results of the loss of mass measurements.

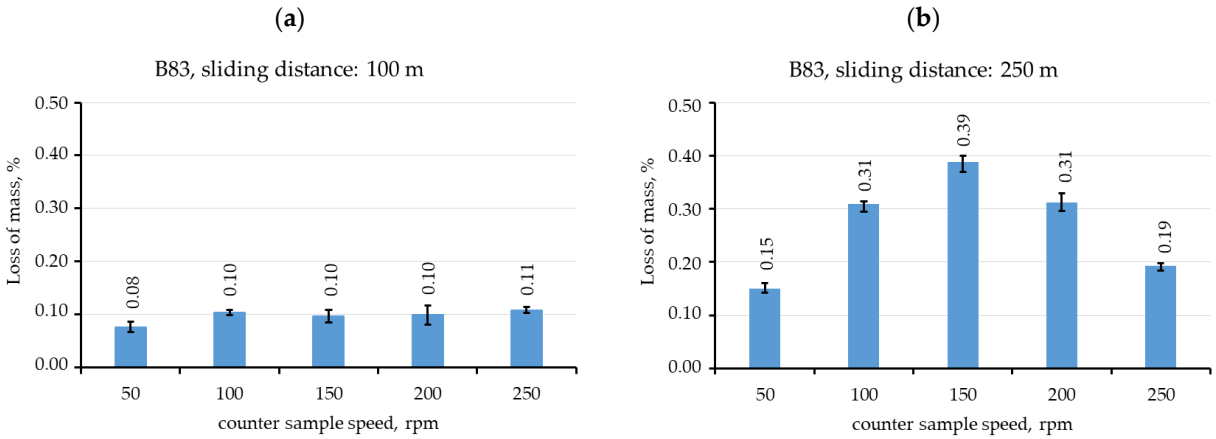

Figure 4. Loss of mass as a function of counter sample speed for B83 alloy: (**a**) sliding distance 100 m; and (**b**) sliding distance 250 m.

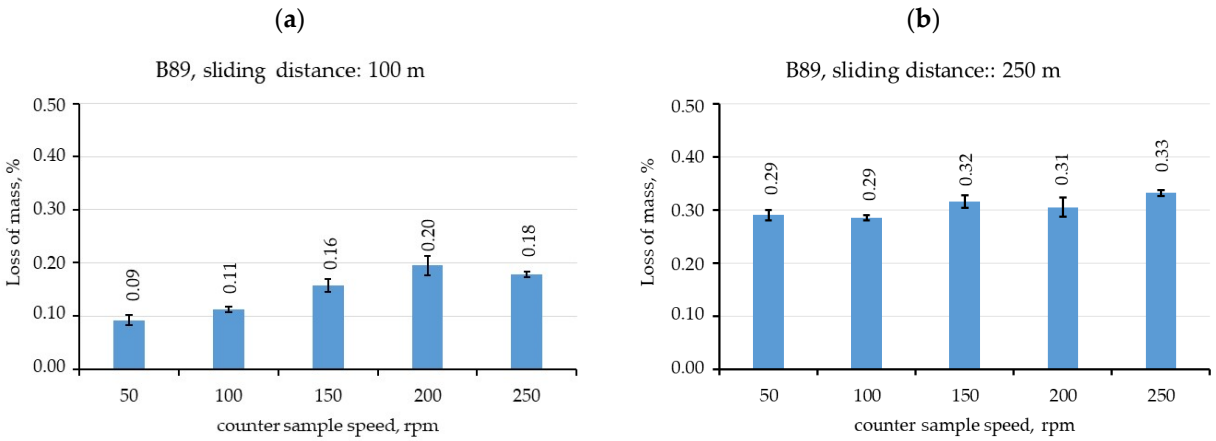

Figure 5. Loss of mass as a function of counter sample speed for B89 alloy: (**a**) sliding distance 100 m; and (**b**) sliding distance 250 m.

Analyzing only the loss of mass, expressed as a percentage reduction in the initial weight of the sample, it can be concluded that the two alloys studied show different susceptibilities to changing process parameters. Alloy B83 shows stable magnitudes of loss of mass at the shorter friction distance; above 100 rpm, the results obtained are within the limit of the measurement error and can therefore be considered representative under these conditions. Increasing the friction distance changes the nature of the results obtained. The function of the loss of mass as a function of the speed of the counter sample takes

on a shape with a maximum which, in our case, is located at 150 rpm. Interestingly, the manufacturer of the device, based on many years of experience, recommends speeds close to this value for universal testing. The key issue here is the approach to the result, which is intended to provide information on 'universal' wear resistance, whether it is determined under mild frictional conditions or those that maximize the frictional mechanisms possible during tribological contact at the friction node. As the alloys differ in microstructure (Figures 2 and 3), it was expected that the alloys would respond differently to the different test conditions. The 100 m distance test for alloy B89 showed that maximum wear was achieved at a counter sample speed of 200 rpm, after which a slight reduction was recorded. The alloy reacts differently over a longer friction distance, with similar results obtained, particularly in the 100 to 150 rpm range. Lower wear was recorded at 50 rpm. Figure 5 summarizes the differences in the results obtained for the two alloys as a function of the friction distance at different speeds, which can be regarded as the so-called 'result stability parameter' S.

The differences in the results obtained, presented in Table 3, show even more clearly that the microstructural characteristics lead to a completely different behavior of the alloys tested in the tribological tests. Alloy B83 is characterized by a three-phase microstructure: a tin-rich matrix with very good sliding properties and two phases with a strengthening character, namely, large rhomboidal and cubic SnSb phase precipitates and many needle-shaped and near globular Cu_6Sn_5 phase precipitates (Figure 2). This type of microstructure is maximally optimized in terms of wear resistance, i.e., the right balance between the coefficient of friction (for which the soft matrix is particularly responsible) and wear resistance. Alloy B89, on the other hand, is characterized by a different type of microstructure; in addition to a soft tin matrix, it has Cu_6Sn_5 phase precipitates, which are needle-like and almost spherical in shape. SnSb precipitates are only sporadic and much smaller than in the case of alloy B83 (Figure 3), so they have less influence on the tribological properties of the alloy. These characteristics result in different behaviors of the tested alloys depending on the applied speed and friction distance.

Table 3. The range of results for individual tests.

Material	Sliding Distance	Spread of Results	S
B83	100 m	34.78%	0.35
	250 m	88.68%	0.89
B89	100 m	71.78%	0.72
	250 m	15.24%	0.15

As the variable parameter other than the material type was the speed, the formula for the wear rate was established according to relation (1), and the calculation results are summarized in Figure 6. The wear rate results indicate how quickly the pan material will wear at different speeds, e.g., the shaft. The correlation between the loss of mass and wear rate was checked, and, for the B83 alloy, which has a three-phase microstructure, the behavior of both parameters was shown to be similar (Figures 4 and 5).

A comparison of the loss of mass presented in Figure 4a,b for alloy B83 reveals a certain convergence in the obtained results. For a friction distance of 250 m, the graphs indicate a maximum wear at rotational speeds of 150 to 200 rpm, followed by a subsequent decrease in a loss of mass as the process progresses and the wear rate stabilizes. In contrast, for a friction distance of 100 m, a continuous increase in loss of mass is observed, while the parameter remains relatively stable. For alloy B89, a continuous increase in the loss of mass is observed, with its stabilization for a 100 m friction distance at rotational

speeds of 200 and 250 rpm (Figure 5a,b). The wear rate analysis highlights the necessity of considering the run-in period of the specimens in test design. During this phase, the removal of surface irregularities occurs, particularly on the harder test material containing carbides. Another significant factor, closely related to the type of tribological contact, is the transition from linear contact at the beginning of the test to diffuse contact as the contact area increases. This transition also affects the distribution of forces at the friction node.

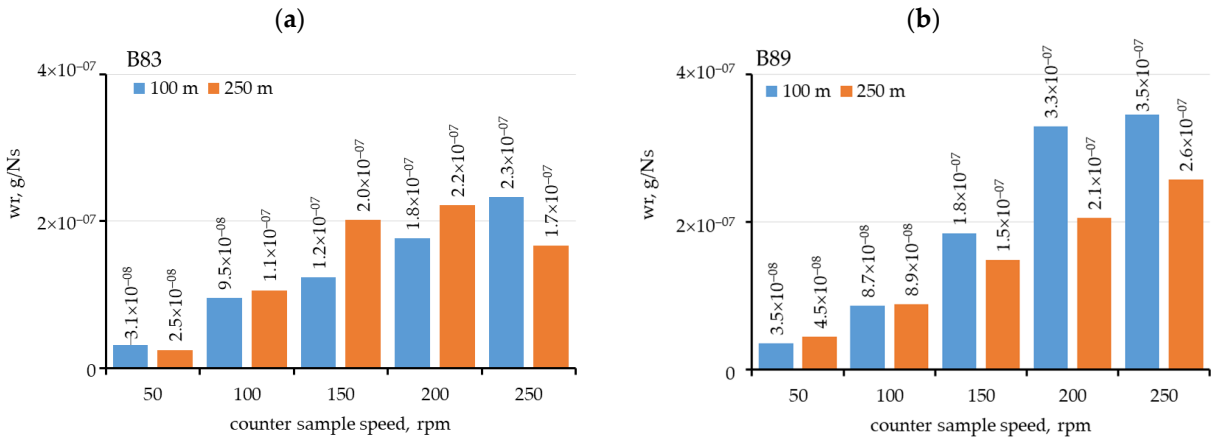

Figure 6. Wear rate of analyzed alloys as a function of sliding distance: (**a**) B83; and (**b**) B89.

The analysis of frictional force during the test enables both the determination of the coefficient of friction and the assessment of changes in wear mechanisms, as well as potential chemical and thermal reactions between the examined material and the defined counter sample under the given frictional conditions. The following graphs (Figures 7 and 8) present the variations in frictional force as a function of test duration.

For alloy B83, the variations in frictional force are presented in Figure 7. It is evident that the rotational speed influences the progression of frictional force in the tested contact pair. The curve can be divided into two stages: the running-in period, which typically lasts from several seconds to approximately 30 s, followed by a steady-state period. However, at a rotational speed of 50 rpm for friction distances of 100 and 250 m, significant fluctuations in frictional force and a notably high coefficient of friction are observed compared to higher spindle speeds. This phenomenon can be explained, on the one hand, by the prolonged tribological contact time between the sliding surfaces and the slower removal of wear products. In the case of harder phase fragmentation, this may lead to the prolonged presence of abrasive particles in the friction node, whereas, at higher speeds, these particles are rapidly removed. Additionally, adhesion effects at lower speeds may necessitate greater force to break the contact. For alloy B83 (Figure 7), dynamic variations in frictional force were observed at a rotational speed of 150 rpm.

Alloy B89 exhibits frictional force variation characteristics similar to those of alloy B83 (Figure 8). At a spindle speed of 50 rpm, significant fluctuations in frictional force are observed, with the force reaching its highest values at this speed.

In all cases (Figures 7 and 8), the frictional force curve for a counter sample rotational speed of 100 rpm exhibits the most well-defined pattern. After the running-in period, a steady-state period is observed, during which the frictional force remains relatively stable throughout the entire test duration. This behavior is characteristic of both alloys, regardless of the friction distance. Furthermore, the tested alloys exhibit different frictional behavior at rotational speeds of 200 and 250 rpm. In the case of alloy B83, the frictional force remains relatively stable after an initial dynamic increase, forming a plateau on the graph. In contrast, alloy B89 shows a continuous increase in frictional resistance regardless of the friction distance, leading to a progressive rise in frictional force as the tribological

test proceeds. These differences can be attributed to the microstructural characteristics of the alloys, particularly the absence of a large rhomboidal and cubic SnSb phase in alloy B89. The shape and distribution of these phases within the soft tin-based matrix appear to play a crucial role at higher sliding speeds. This observation aligns with trends in the market for sliding materials, where alloy B83 is significantly more popular for bearing overlay applications.

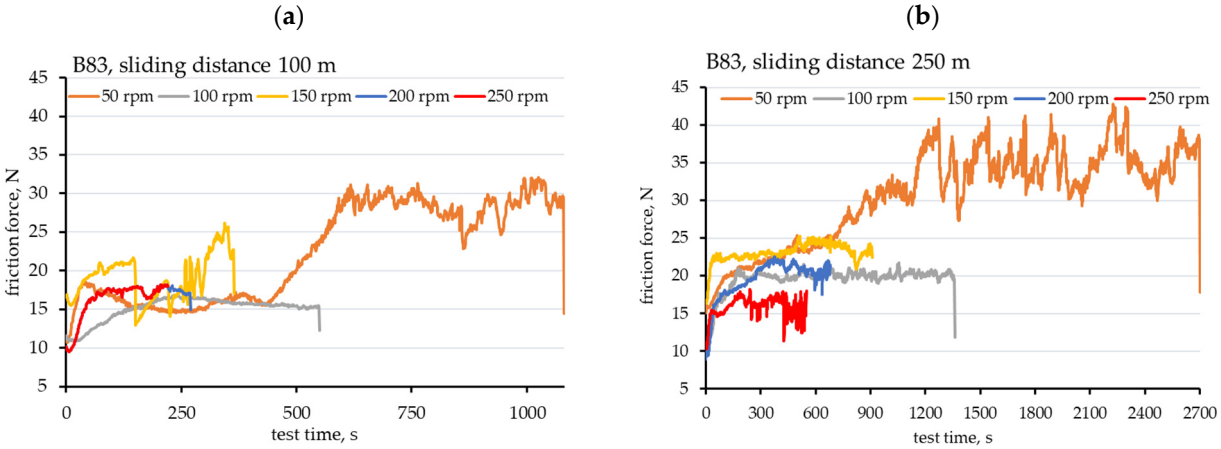

Figure 7. Friction force of the B83 alloys as a function of time and counter sample speed: (**a**) sliding distance of 100 m; and (**b**) sliding distance of 250 m.

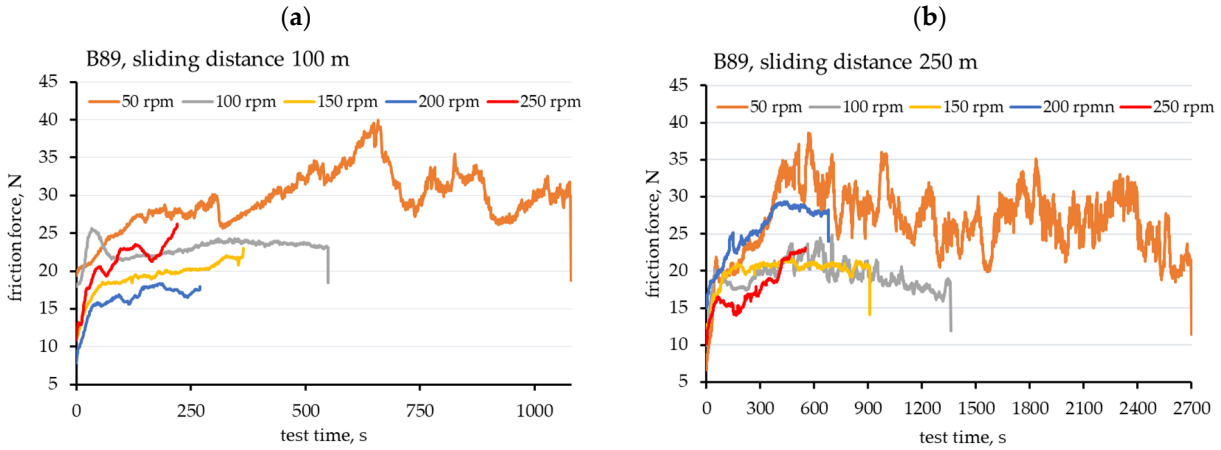

Figure 8. Friction force of the B89 alloys as a function of time and counter sample speed: (**a**) sliding distance of 100 m; (**b**) sliding distance of 250 m.

The authors of this study have also highlighted the potential for improving the properties of alloy B83 through heat treatment or the Friction Stir Processing Method (FSP), which modifies the morphology of the precipitates [30]. To further illustrate these findings, the average coefficients of friction for the entire test process have been determined and are presented in the table below (Table 4).

The results presented in Table 4 confirm that low rotational speeds under technically dry friction conditions are highly unfavorable for both alloys. The variation in frictional force and the average coefficient of friction significantly deviate from the characteristics desirable for sliding materials, aside from extreme operating conditions. Since the tests were conducted in technically dry friction conditions, they provide valuable insights into the alloys' resistance to lubrication system failures or interruptions in lubricant supply.

Table 4. Coefficient of friction.

Material	rpm	Coefficient of Friction	
		100 m	250 m
B83	50	0.393	0.540
	100	0.265	0.343
	150	0.335	0.405
	200	0.288	0.343
	250	0.284	0.278
B89	50	0.519	0.469
	100	0.404	0.347
	150	0.338	0.353
	200	0.286	0.448
	250	0.448	0.430

At higher rotational speeds, a reduction in the coefficient of friction is observed for alloy B83, whereas, for alloy B89, the average coefficient of friction increases, particularly with an extended friction distance. This trend can be attributed to the absence of the friction-stabilizing SnSb phase in alloy B89. The analysis of both friction force variation over time (Figures 7 and 8) and the average coefficients of friction (Table 4) indicates that differences in chemical composition—specifically the presence of an additional SnSb phase in alloy B83—alter the alloy's frictional behavior.

To further validate these observations, the friction surfaces of the tested alloys were examined. Selected examples of the surface morphology of both alloys under dry friction conditions are presented in Figures 9–11. The results indicate that, at a spindle speed of 50 rpm, the dominant wear mechanism is abrasive wear, primarily characterized by scratching and furrowing of the material surfaces. This is influenced by the nature of the 100Cr6 steel counter sample, which contains protruding $Cr_{23}C_6$ carbides that are significantly harder than both tested alloys, as well as the potential spalling of Cu_6Sn_5 phases. These spalled particles may act as abrasives within the friction node for an extended period.

At low rotational speeds, the removal of detached particles from the friction node is inefficient, exacerbating wear processes. The presence of abrasives significantly accelerates material degradation, highlighting the importance of designing friction nodes to facilitate the rapid removal of high-hardness particles from at least one of the materials involved in friction.

The analysis of the friction surface of the B83 alloy (Figures 9a and 10a) reveals the presence of transverse cracking, material transfer, and smearing, in addition to localized abrasive wear observed in the tin-rich matrix regions. The movement of the matrix along the surface is impeded by large rhomboidal SnSb precipitates. In the B89 alloy, additional phenomena related to material attrition are observed, with inhibition effects caused by precipitates and clusters of presumed oxides, which tend to accumulate in areas where intense abrasion is not present (Figures 9b and 10b). The presence of oxides on the friction surface has been confirmed in previous studies, as reported in the study of [24]. At a low spindle speed (Figure 9a), fatigue cracking is minimal and difficult to detect within the tribological contact area. The accumulation of material around SnSb precipitates leads to significant surface irregularities (Figure 9a, 3D profile), which may facilitate continuous smearing of these precipitates across the surface and contribute to the pronounced variations in frictional force during testing. This effect may also be associated with the shortening of possible adhesion bonds; however, the high ductility of tin and its tendency to undergo plastic deformation prevent the formation of typical adhesion marks on the surface.

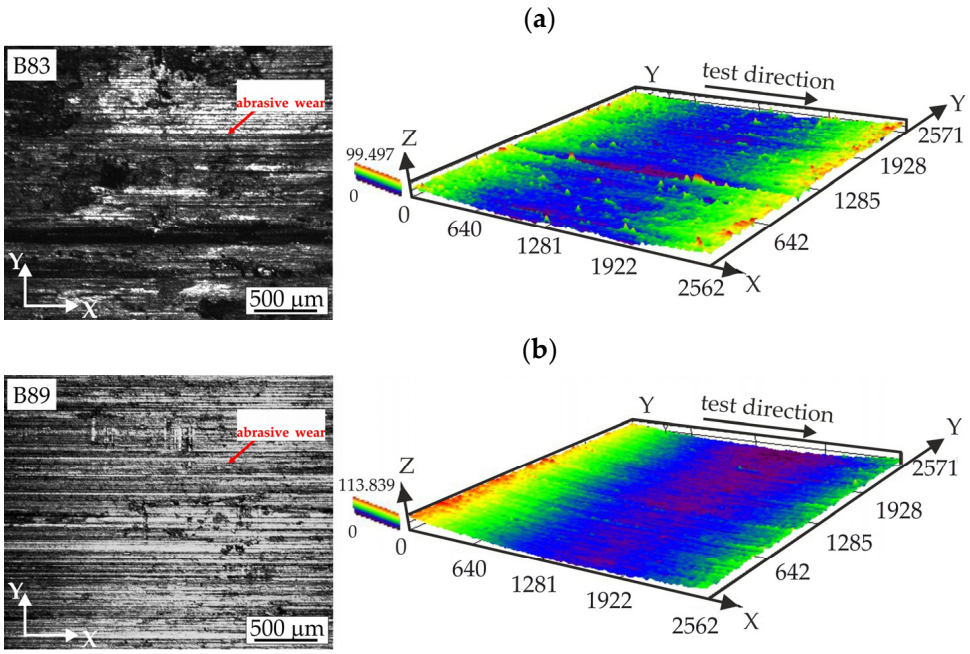

Figure 9. Surface morphology of tested alloys after sliding contact under technical dry friction: (**a**) 2D view and 3D view of B83 after examining on 250 m with rotational speed of 50 rpm; (**b**) 2D view and 3D view of B89 after examining on 250 m with rotational speed of 50 rpm.

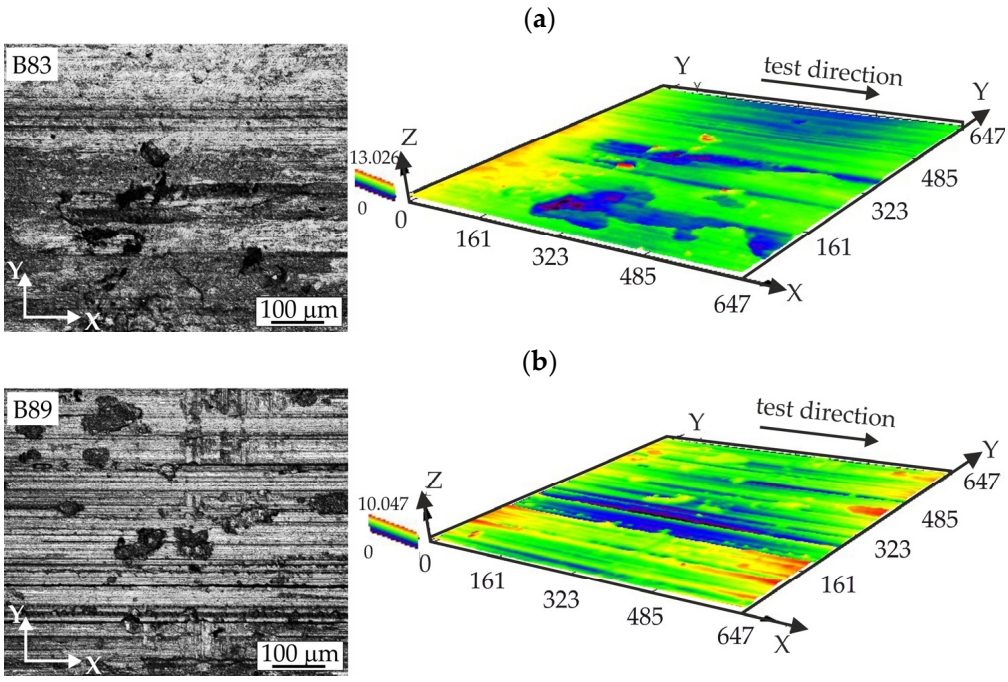

Figure 10. Surface morphology of tested alloys after sliding contact under technical dry friction: (**a**) 2D view and 3D view of B83 after examining on 250 m with rotational speed of 250 rpm; and (**b**) 2D view and 3D view of B89 after examining on 250 m with rotational speed of 250 rpm.

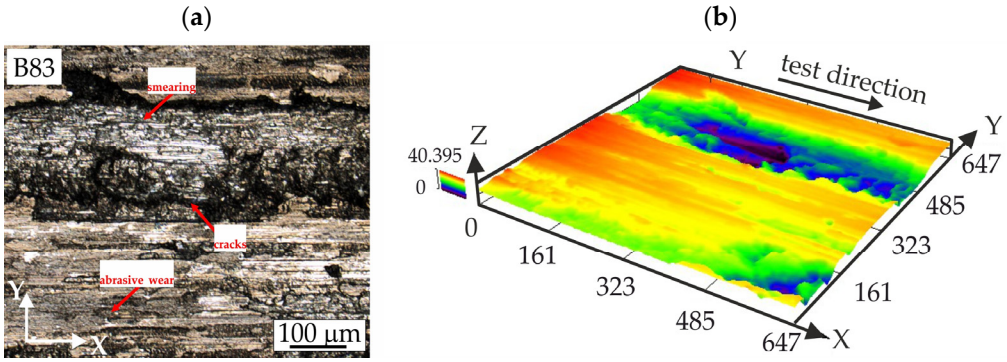

Figure 11. Surface morphology after sliding contact under technically dry friction; B83 alloy after examining on 250 m with rotational speed of 150 rpm: (**a**) 2D view; and (**b**) 3D view.

At increased spindle speeds (Figure 10a), smearing of the matrix material is also observed, with tin-rich streaks aligned with the direction of counter sample rotation. The effects of abrasive wear become less pronounced due to the high-intensity smearing of the matrix material. The formations present on the surface are more indicative of Cu_6Sn_5 phase chipping rather than matrix material removal. Fine oxides are also visible, though their quantity is lower compared to samples subjected to friction at 50 rpm.

This rotational speed also contributes to the intensification of fatigue processes, as evidenced by the presence of numerous fatigue-like cracks. While these cracks are generally oriented transversely to the direction of friction, some appear at a 45° angle to the reciprocal rotation direction of the specimen and counter sample.

The analysis of the surface topography presented in the 3D view (Figure 10a) indicates that most of the observed craters in this alloy can be attributed to the chipping of the Cu_6Sn_5 phase, with the detachment of these particles accompanied by surface scratching until their complete removal from the friction node. The three-dimensional surface mapping also confirms the presence of a depression on the friction surface, corresponding to the shape of the counter sample, though with a relatively shallow depth.

At a spindle speed of 250 rpm, the frictional force exhibits a steadily increasing trend, suggesting that matrix fatigue, localized fatigue due to intensive plastic deformation, and the progressive failure of adhesion bonds intensify over time. This progression could ultimately lead to seizure within the friction node under prolonged operation. The craters observed on the surface resemble those characteristic of fretting wear; however, no evidence of accelerated corrosion is present in these regions.

Alloy B89 demonstrates distinct behavior under the same friction conditions compared to alloy B83. Regardless of spindle speed, abrasive wear is the predominant friction mechanism. The friction surfaces predominantly display scratches and grooves, resulting from the presence of hard $Cr_{23}C_6$ carbides on the surface of the 100Cr6 steel counter sample, which cut into the B89 test material. Additionally, craters likely caused by the chipping of Cu_6Sn_5 phase particles are observed. The occurrence of these chipping craters is closely linked to the friction velocity—on the surface shown in Figure 9b, only a few small craters are present, whereas, in the material tested at 250 rpm (Figure 10b), these craters are more numerous and cover a larger area of the analyzed friction surface. On the surface subjected to friction at 50 rpm, clusters of oxides that have not chipped off and remain on the surface can also be observed. At a speed of 250 rpm (Figure 10b), surface spalling is evident, likely caused by the chipping of Cu_6Sn_5 hard phase particles. This phenomenon alters the contact surface during displacement and induces dynamic interactions between the friction surfaces under a continuous load of 50 N. As a result of these interactions, characteristic signs of fatigue wear appear, leading to localized material loss perpendicular to the direction of friction, although this results in only minor material loss in this region.

However, an overview of the wear patterns of the B89 alloy, as depicted in the 3D view, clearly shows that the Cu_6Sn_5 particles offer limited resistance to abrasive wear. This leads to typical semicircular abrasion on the test alloy surface, with a greater depth than observed for alloy B83 tested at 50 rpm. Increasing the rotational speed modifies the friction mechanisms described above, resulting in a more complex surface morphology. Instead of forming a uniform semicircular cavity, the surface adopts a more intricate shape influenced by localized wear mechanisms, without the dominance of abrasive wear throughout the entire friction node.

Since the maximum frictional wear of the B83 alloy was observed at 150 rpm, the friction surface for this variant is also analyzed (Figure 11).

At this spindle speed, over a friction distance of 250 m, mechanisms other than abrasive wear become dominant. The displacement of matrix material, numerous fatigue cracks, and a locally significant presence of fretting are observed. Additionally, oxides accumulate in depressions, remaining on the surface despite the high sliding velocity.

The presence of these mechanisms indicates intense plastic interaction between the friction surfaces. This effect results from a velocity that is insufficient to eliminate material smearing while simultaneously being too high for abrasive wear to dominate. In the analyzed surface (Figure 11), abrasive wear is observed only in micro-regions of the intact matrix, where it is constrained by the existing strengthening phases in the material (Cu_6Sn_5 and SnSb). Increasing the rotational speed of the counter sample intensifies the smearing of the tin-rich matrix, allowing the closure of fretting grooves. This inhibits the fretting mechanism and leads to a reduction in the sample's loss of mass.

4. Summary and Conclusions

The objective of this study was to determine the effect of friction process parameters, represented by the counter sample rotational speed and friction distance, on wear resistance and the coefficient of friction. The investigation was conducted on two alloys, B83 and B89, which are dedicated to applications as sliding materials. The tests were performed using a T-05 universal block-on-ring tribotester, which differs significantly from the more commonly used ball-on-disk and pin-on-disk testers found in laboratories.

With a broad range of available material testing methods, adapting a test to specific needs is relatively straightforward when relying on the literature data and existing test result databases, facilitating comparisons. Roller-block configurations, which are more versatile and allow testing in the presence of lubricants, are also utilized in research laboratories. However, the available dataset for this method is significantly smaller than for the previously mentioned techniques. As a result, designing a tribological test based on the roller-block system often requires reference to industrial applications or the selection of universal test conditions. The present study aims to address this question: what are the universal conditions for testing in a block-on-ring configuration?

To answer this, materials with distinctly different microstructures, and thus different behavior during testing, were analyzed under varying spindle speeds, with friction distances of 100 m and 250 m. The primary parameter examined was loss of mass, as it serves as a fundamental indicator for comparing wear resistance.

For the B83 alloy, which has a three-phase microstructure, the results for a 100 m friction distance were similar across all spindle speeds, except for the lowest speed. However, extending the friction distance led to a distinct peak in the loss of mass at a counter sample rotational speed of 150 rpm, coinciding with the highest coefficient of friction (except at 50 rpm). The loss of mass decreased at both lower and higher speeds. Similarly, the wear rate at 150 rpm was the highest (comparable to 200 rpm), suggesting that, from the

perspective of wear severity, the most critical friction conditions occur at 150 rpm. Under these conditions, both wear and the coefficient of friction reach their maximum values.

This observation indicates that, in alloys with a soft matrix and two types of strengthening phases—such as B83, which contains large rhomboidal and cubic SnSb phase precipitates along with numerous needle-like and nearly globular Cu_6Sn_5 precipitates—testing with a 100Cr6 steel counter sample at approximately 150 rpm provides the maximum wear response. This insight helps assess how materials with properties similar to B83 bearing alloy perform under severe friction conditions. The loss of mass determined under these conditions was higher than that of the B89 alloy tested at its maximum speed.

In contrast, the B89 alloy, which exhibits a typical two-phase microstructure with only a few very fine SnSb precipitates, does not allow for conclusions different from those drawn for B83. An increase in rotational speed results in greater wear, largely independent of friction distance. The coefficient of friction does not follow a clear trend (Table 4); however, when excluding the lowest speed of 50 rpm, an increasing tendency is also observed. This is further confirmed by the wear rate trends shown in Figure 6, where the wear rate increases proportionally to material wear.

Interestingly, in the case of B89, wear occurs primarily through abrasive mechanisms, with only a minor contribution from the initial stages of spalling. This suggests that the distribution of the strengthening phase in this alloy is beneficial for wear resistance at low rotational speeds. However, when evaluating this material under severe conditions, the rotational speed of the test should be increased as much as the test apparatus allows.

Author Contributions: Conceptualization, M.M.; methodology, M.M. and B.L.-M.; formal analysis, M.M. and B.L.-M.; investigation, M.M. and B.L.-M.; writing, M.M.; writing—review and editing, M.M. and B.L.-M.; visualization, M.M. and B.L.-M. All authors have read and agreed to the published version of the manuscript.

Funding: This research received no external funding.

Data Availability Statement: The original contributions presented in the study are included in the article, further inquiries can be directed to the corresponding author.

Conflicts of Interest: The authors declare no conflicts of interest.

References

1. Li, D.; Leroux, P. Block on Ring Sliding Wear Evaluation. *Nanovea Broch.* **2016**. Available online: https://www.researchgate.net/profile/Duanjie-Li/publication/309491420_Block_on_Ring_Sliding_Wear_Evaluation/links/581365c308aedc7d8961e08d/Block-on-Ring-Sliding-Wear-Evaluation.pdf (accessed on 3 February 2025).
2. Findik, F. Latest Progress on Tribological Properties of Industrial Materials. *Mater. Des.* **2014**, *57*, 218–244. [CrossRef]
3. Tewari, A. Load Dependence of Oxidative Wear in Metal/Ceramic Tribocouples in Fretting Environment. *Wear* **2012**, *289*, 95–103. [CrossRef]
4. Chavhan, G.R.; Wankhade, L.N. Optimization of Test Parameters that Influence on Dry Sliding Wear Performance of Steel Embedded Glass/Epoxy Hybrid Composites by Using the Taguchi Approach. *Tribol. Ind.* **2020**, *42*, 556–571. [CrossRef]
5. Birleanu, C.; Pustan, M.; Pop, G.; Cioaza, M.; Popa, F.; Lazarescu, L.; Contiu, G. Experimental Investigation of the Tribological Behaviors of Carbon Fiber Reinforced Polymer Composites under Boundary Lubrication. *Polymers* **2022**, *14*, 3716. [CrossRef]
6. Muratov, V.A.; Luangvaranunt, T.; Fischer, T.E. The Tribochemistry of Silicon Nitride: Effects of Friction, Temperature and Sliding Velocity. *Tribol. Int.* **1998**, *31*, 601–611. [CrossRef]
7. Rymuza, Z.; Pytko, S. The Effect of Scale in Tribological Testing. *J. Mater. Res. Technol.* **2012**, *1*, 13–20. [CrossRef]
8. Sundararajan, S.; Bhushan, B. Micro/Nanoscale Tribology of MEMS Materials, Lubricants and Devices. In *Fundamentals of Tribology and Bridging the Gap Between the Macro- and Micro/Nanoscales*; Bhushan, B., Ed.; NATO Science Series: Dordrecht, The Netherlands, 2001; Volume 10. [CrossRef]
9. Kagnaya, T.; Boher, C.; Lambert, L.; Lazard, M.; Cutard, T. Wear Mechanisms of WC–Co Cutting Tools from High-Speed Tribological Tests. *Wear* **2009**, *267*, 890–897. [CrossRef]

10. Zhen, J.; Zhu, S.; Cheng, J.; Qiao, Z.; Liu, W.; Yang, J. Effects of Sliding Speed and Testing Temperature on the Tribological Behavior of a Nickel-Alloy Based Solid-Lubricating Composite. *Wear* **2016**, *368–369*, 45–52. [CrossRef]
11. Jansons, E.; Lungevics, J.; Kanders, U.; Leitans, A.; Civcisa, G.; Linins, O.; Kundzins, K.; Boiko, I. Tribological and Mechanical Properties of the Nanostructured Superlattice Coatings with Respect to Surface Texture. *Lubricants* **2022**, *10*, 285. [CrossRef]
12. Guezmil, M.; Bensalah, W.; Khalladi, A.; Elleuch, K.; De-Petris Wery, M.; Ayedi, H.F. Effect of Test Parameters on the Friction Behaviour of Anodized Aluminium Alloy. *Int. Sch. Res. Not.* **2014**, *1*, 2356–7872. [CrossRef]
13. Zeren, A.; Feyzullahoglu, E.; Zeren, M. A study on the tribological behaviour of tin-based bearing material in dry sliding. *Mater. Des.* **2007**, *28*, 318–323. [CrossRef]
14. Alcover, P.R.C., Jr.; Pukasiewicz, A.G.M. Evaluation of microstructure, mechanical, and tribological properties of a Babbitt alloy deposited by arc and flame spray processes. *Tribol. Int.* **2019**, *131*, 148–157. [CrossRef]
15. Wu, H.; Bi, Q.; Zhu, S.; Yang, J.; Liu, W. Friction and wear properties of Babbitt alloy 16-16-2 under seawater environment. *Tribol. Int.* **2011**, *44*, 1161–1167. [CrossRef]
16. Ünlü, B.S. Investigation of tribological and mechanical properties of metal bearings. *Bull. Mater. Sci.* **2019**, *32*, 451–457. [CrossRef]
17. Ren, X.; Chen, N.; Zhang, G.; Xu, H.; Zhang, Y.; Shi, Z.; Wang, Z.; Liu, Y. Effect of Pb on microstructure and mechanical properties of tin Babbitt alloy. *J. Phys. Conf. Ser.* **2023**, *2478*, 052007. [CrossRef]
18. Choudhary, P.; Brar, G.S.; Sharma, V. Experimental study and numerical simulation of tribological and mechanical properties of mullite and SiC ceramic matrix composite for journal bearing. *Proc. Inst. Mech. Eng. Part J J. Eng. Tribol.* **2025**. [CrossRef]
19. Bykov, P.A.; Kalashnikov, I.E.; Kobeleva, L.I.; Katin, I.V.; Mikheev, R.S. Wear regimes of hot-extruded Babbitt-based composites. *Inorg. Mater.* **2024**, 1–9. [CrossRef]
20. Bolotova, L.; Kalashnikov, I.; Kobeleva, L.; Bykov, P.; Katin, I.; Kolmakov, A.; Podymova, N. Structure and properties of the B83 Babbitt alloy-based composite materials produced by extrusion. *Inorg. Mater. Appl. Res.* **2018**, *9*, 478–483. [CrossRef]
21. Song, H.; Wang, M.; Zhang, D.; Zhang, G.; Wen, K.; Zhang, Y.; Xia, J.; Miao, X.; Xu, H. Analysis of interface bonding mechanism of Babbitt alloy/steel compound castings with different surface treatments. *Metals* **2024**, *14*, 1201. [CrossRef]
22. Ni, Y.; Zhang, H.; Dong, G. Tribological performances of modified Babbitt alloy under different sliding modes. *ASME J. Tribol.* **2021**, *143*, 061402. [CrossRef]
23. Branagan, L.A. Survey of damage investigation of Babbitted industrial bearings. *Lubricants* **2015**, *3*, 91–112. [CrossRef]
24. Madej, M.; Leszczyńska-Madej, B. Analysis of the effect of the chemical composition of bearing alloys on their wear under wet friction conditions. *Lubricants* **2023**, *11*, 426. [CrossRef]
25. *ASTM E10-18*; Standard Test Method for Brinell Hardness of Metallic Materials. ASTM International: West Conshohocken, PA, USA, 2017.
26. Leszczyńska-Madej, B.; Madej, M.; Hrabia-Wiśnios, J. Effect of chemical composition on the microstructure and tribological properties of Sn-based alloys. *J. Mater. Eng. Perform.* **2019**, *28*, 4065–4073. [CrossRef]
27. Barykin, N.P.; Sadykov, F.A.; Aslanyan, I.R. Wear and failure of babbit bushes in steam turbine sliding bearings. *J. Mater. Eng. Perform.* **2000**, *9*, 110–115. [CrossRef]
28. Valeeva, A.K.; Valeev, I.S.; Fazlyakhmetov, R.F. On the Wear Rate of an Sn11Sb5.5Cu Babbitt. *J. Frict. Wear* **2017**, *38*, 53–57. [CrossRef]
29. Potekhin, B.A.; Il'yushin, V.V.; Khristolyubov, A.S. Effect of casting methods on the structure and properties of tin babbit. *Met. Sci. Heat. Treat.* **2009**, *51*, 378–382. [CrossRef]
30. Madej, M.; Leszczyńska-Madej, B.; Hrabia-Wiśnios, J.; Węglowska, A. Effect of FSP on Tribological Properties of Grade B89 Tin Babbitt. *Materials* **2021**, *14*, 2627. [CrossRef]
31. Goudarzi Moazami, M.; Jenabali Jahromi, S.A.; Nazarboland, A. Investigation of characteristics of tin-based white metals as a bearing material. *Mater. Des.* **2009**, *30*, 2283–2288. [CrossRef]